Icarus 279 (2016) 51–61

Contents lists available at ScienceDirect

Icarus

journal homepage: www.elsevier.com/locate/icarus

In-situ measurements of Saturn's dusty rings based on dust impact signals detected by Cassini RPWS

S.–Y. Ye*, D.A. Gurnett, W.S. Kurth

Department of Physics and Astronomy, The University of Iowa, Iowa City, IA, USA

ARTICLE INFO

Article history:
Received 11 May 2015
Revised 25 April 2016
Accepted 1 May 2016
Available online 13 May 2016

Keywords:
Saturn rubgs
Enceladus
Impact processes

ABSTRACT

The Cassini Radio and Plasma Wave Science (RPWS) instrument can detect dust particles when voltage pulses induced by the dust impacts are observed in the wideband receiver. The size of the voltage pulse is proportional to the mass of the impacting dust particle. In this paper, we show RPWS measurements of dust particles in Saturn's dusty rings. The differential size distribution of the dust particles can be characterized as a power law $dn/dr \propto r^{\mu}$, where $\mu \sim -4$ and r is the particle radius. The observed particle radius ranged from 0.2 to 10 μm. The dust density profiles of the dusty rings are derived from the impact rates measured by the RPWS wideband receiver. The radial density profiles show peaks near Enceladus' orbit and the G ring. The region around the G ring is found to be a very thin layer of dust particles with no observable vertical offset of the peak density from the ring plane. The vertical scale height of the E ring varies with the radial distance from Saturn with a local minimum at Enceladus' orbit. The vertical density profiles of the E ring show dips at the equatorial plane near Enceladus' orbit and vertical offsets of the peak locations away from Enceladus' orbit. These observations are consistent with previous modeling studies and measurements by other instruments onboard Cassini.

1. Introduction

The planet Saturn is surrounded by the most spectacular ring system in the Solar System. The main rings, which are located within the Roche limit of the planet, consist of centimeter to meter size ice particles (Zebker et al., 1985; Tiscareno, 2013). Although the main rings of Saturn are enormous in size (diameter~270,000 km), their thickness does not exceed 100 m (Zebker and Tyler, 1984). Fainter rings, namely G, E and Phoebe rings, have been discovered outside the main rings (Feibelman, 1967; Van Allen et al., 1980; Smith et al., 1981; Verbiscer et al., 2009). These dusty rings consist mainly of dust particles from nanometers to 10 s of micrometers in size (Showalter et al., 1991; Showalter and Cuzzi, 1993; Throop and Esposito, 1998; de Pater et al., 2004; Spahn et al., 2006a and b; Hedman et al., 2007; Kempf et al., 2008; Hamilton et al., 2015). These small particles are subject to additional forces beyond gravity (e.g. solar radiation pressure), and thus their behavior is more complicated and often significantly different from that of the larger particles in the main rings (Horanyi, 1996). These additional forces can lead to very rapid evolution, and thus short lifetimes of the dust particles, which requires a corresponding production of dust to balance these losses. It has been discovered by Cassini that the cryovolcanic activity near the south pole of Enceladus is responsible for supplying the material in the E ring (Waite et al., 2006; Spahn et al., 2006b; Porco et al., 2006). Meteoroid impacts into, and collisions among, the small bodies and moonlets within the G ring arc are found to be responsible for generation of the dusty G ring (Hedman et al., 2007).

Wang et al. (2006) and Kurth et al. (2006) reported the in-situ measurements of dust impacts by the Cassini Radio and Plasma Wave Science (RPWS) wideband receiver during the Saturn orbit insertion (SOI) and E ring crossings respectively. These studies show that the differential size distribution of the dust particles detected during the SOI and E ring crossings can be characterized as a power law $dn/dr \propto r^{\mu}$, where $\mu \sim -4$ to -6, and r is the particle radius. The impact rates measured by the wideband receiver can be converted to dust density based on an estimate of the effective impact area of the spacecraft.

Dust particles have also been detected in-situ by the dedicated dust detector onboard Cassini, the Cosmic Dust Analyzer (CDA) (Srama et al. 2004). CDA is designed to measure the size, density, velocity, charge and composition of the dust particles. Thus although it was shielded by the High Gain Antenna during the SOI and could not detect the dust particles, CDA data collected during the following ring plane crossings (with calibrated size thresholds and effective detection areas) can be used to calibrate the result of

* Corresponding author. Tel.: +1 3193351699.
E-mail address: shengyi-ye@uiowa.edu (S.–Y. Ye).

http://dx.doi.org/10.1016/j.icarus.2016.05.006
0019-1035/

RPWS measurements (Spahn et al., 2006a; Kempf et al., 2008; Ye et al., 2014). Kempf et al. (2012) reconstructed the 3 dimensional morphology of the E ring from vertical and equatorial dust density profiles measured by the CDA. They found that the radial density profile of the E ring is dependent on the local time, which was also seen in the imaging data (Hedman et al., 2012).

The dusty rings of Saturn can also be measured by the remote sensing instruments onboard Cassini, e.g., Imaging Science Subsystem (ISS) and Visual and Infrared Mapping Spectrometer (VIMS). Ingersoll and Ewald (2011), based on ISS observation, determined the median radius of the dust particles (assuming spherical shape) in the Enceladus plume to be 3.1 μm. They also estimated the total mass of particles in the Enceladus plume and E ring and deduced the lifetime of the dust particles in the E ring to be ~8 years. Horanyi et al. (1992) and Hamilton (1993) modeled the motion of dust particles in the E ring and predicted radial and vertical structures of the E ring confirmed by later Cassini observations. Hedman et al. (2009) deduced the dust density profile and the velocity distribution of particles launched from the south pole of Enceladus based on the VIMS observations of the plume. Based on ISS images, Hedman et al. (2012) showed that E ring's vertical thickness grows with distance from Enceladus' orbit and the E ring's peak density shifts from south to north of Saturn's equator plane with increasing radial distance from Saturn. The ISS data also revealed a localized depletion in particle density near Saturn's equatorial plane around Enceladus' orbit. These characteristics of the E ring's structure are the result of a combination of external forces acting on the dust particles changing their trajectory around the planet. This density depletion near the ring plane was also observed by RPWS during the E ring crossing (Kurth et al., 2006) but not clearly detected in CDA measurements (Kempf et al., 2008, 2010).

In this paper, we analyze Cassini RPWS data collected during the ring plane crossings (within 6 R_S) between the SOI (07-01-2004) and equinox (08-11-2009) (high inclination ring plane crossings analyzed in this study are listed in Table 1). We apply an updated dust detection algorithm and data analysis method (Ye et al., 2014) to the data analyzed by Wang et al. (2006) and Kurth et al. (2006). In Section 2, we briefly describe the RPWS dust detection mechanism. In Section 3, we show some data collected by RPWS, e.g. ring particle size distributions and dust density profiles of the dusty rings inferred from the dust impact rates. In Section 4, we compare RPWS observations with previous modeling and experimental studies of the dusty rings. In Section 5, we summarize the main results presented in this paper.

2. Detection mechanism

Impact ionization is believed to be the basis for converting the impact energy to an electrical signal (Gurnett et al., 1983; Aubier et al., 1983; Meyer-Vernet 1985). When a dust particle strikes the spacecraft with high enough impact speed, the kinetic energy involved vaporizes the dust particle and part of the spacecraft surface material. This results in a hot ionized gas with electrons expanding away from the impact site faster than ions if the spacecraft is not charged. The charge Q in the expanding plasma cloud depends on the mass and velocity of the impacting dust grain. In this study, we use the experimentally measured charge yield relation of iron particles impacting the surface material of the Cassini spacecraft and the RPWS electric antenna boom (Collette et al., 2014), while the particles in the dusty rings are mostly ice. The charge yield of ice particles could be significantly lower than iron particles (Timmermann and Grün, 1991). However, the charge yield will increase significantly if there are salts in the ice matrix. The measured charge yield for iron particles is

$$Q/m = 0.0025 \times v^{4.6} \quad (1)$$

for impacts on Kapton, the material of the thermal blanket and

$$Q/m = 0.012 \times v^{3.8} \quad (2)$$

for impacts on Beryllium copper (BeCu), the material of RPWS electric antenna boom, where Q is expressed in Coulombs, m in kilograms and v in km/s. At 10 km/s impact speed, the charge yield relations above both give ~80 fC/pg, which is about 5 times smaller than the relation used in Ye et al. (2014).

Oberc (1996) summarized the different scenarios by which dust impacts can generate electric signals on an electric antenna. Gurnett et al. (1983) proposed that the electric signal observed during a dust impact is the abrupt change in potential difference between the spacecraft and the electric antenna (monopole mode) or two antenna elements (dipole mode), most likely due to differential charge collection by these units. Tsurutani et al. (2004) interpreted the signal observed on the dipole antenna as induced by the electric field caused by the separation of the charges from the dust impact. It is also likely that the signals observed are due to capacitive coupling between the antennas and the impact separated charges. Experimental effort has been devoted to reproducing dust-induced antenna signals using the IMPACT accelerator at LASP University of Colorado. It is found that the charge recollection by either the spacecraft or the antenna can explain some of the dust impact signals and a particular fast antenna signal might be induced by the charge separation in the expanding plasma cloud created by the impact (Collette et al., 2015). A detailed discussion of the scenarios proposed for the generation of dust impact signals can be found in Ye et al. (2014). The choice of antenna mode (either monopole or dipole mode) turns out to have a significant impact on the efficiency of charge collection and the resulting voltage signal level (Meyer-Vernet et al., 2014; Ye et al., 2014). RPWS has three electric antenna booms. The wideband receiver can measure the potential difference between two of the booms (dipole) or between one of the booms and the spacecraft body (monopole) (Gurnett et al., 2004).

For the monopole mode, recollection of impact charges by the spacecraft body or antenna (whichever is impacted) is responsible for the voltage pulses detected. The size of the voltage pulse measured in the receiver is proportional to the charge released from the impact,

$$V = Q/C \quad (3)$$

where C ~200 pF is the total capacitance of the circuit where the both the spacecraft and the antenna boom (with a base capacitance between them) are capacitively coupled to space (Gurnett, 1998; Gurnett et al., 2004). For this study, we assume all ions generated during the impact are recollected by the surfaces impacted on, which are negatively charged within 10 R_S of Saturn's center (Wahlund et al., 2005; Sittler et al., 2006). Collette et al. (2015) showed that a target with a biased potential recollects most of the charges released from a dust impact.

For the dipole mode, Gurnett et al. (1987) proposed that the dust impact signals are results of differential charging of the electric antenna elements by charges released by impacts on the spacecraft body. Therefore, the charge recollection efficiency is greatly reduced due to the smaller collecting area of the electric antenna compared to the spacecraft body. Tsintikidis et al. (1994) showed that the voltage spectrum due to the dust impacts measured by the Voyager PRA monopole antenna is 30-50 times stronger than that measured by the PWS dipole antenna (their Table 1), which led to the conclusion that the dipole antenna is ~40 times less sensitive to dust impacts than that the monopole

Table 1
Data from all Cassini high inclination RPXs between DOY 122, 2005 and DOY 223, 2009 (all collected in dipole mode). Listed are time stamps (SCET), fitting parameters n_0 (fitted peak density for particles with radius > 1 μm), w (fitted half width half maximum), z_0 (fitted vertical offset of the peak from ring plane), and spacecraft locations r_{max} (radial distance from Saturn center), x_{max}, y_{max} (coodinates in the Saturn equatorial frame), LT (local time) at the density peaks of the ring plance crossings. The density unit is m^{-3} and the length unit is R_S (1 R_S = 60,330 km).

Time	n_0	w	z_0	r_{max}	x_{max}	y_{max}	LT
SCET	m^{-3}	R_S	R_S	R_S	R_S	R_S	Hour
2005-05-02T23:33:20	0.030705	0.036021	−0.00785	3.901143	0.717022	3.841845	17.3
2005-06-08T08:25:47	0.016951	0.03379	0.007732	3.907838	0.815206	3.828093	17.2
2005-06-26T13:31:15	0.032706	0.032514	−0.00104	3.93517	0.854308	3.831623	17.2
2005-08-02T03:32:35	0.01935	0.034796	−0.00584	3.952776	1.003168	3.818482	17
2005-08-20T08:56:57	0.04145	0.033234	−0.00338	3.932804	1.098233	3.789697	16.9
2006-09-09T19:06:22	0.001593	0.08558	−0.01654	3.151713	2.585931	1.81989	14.3
2006-09-25T22:19:22	0.006149	0.043779	0.001757	4.350887	3.58728	2.460442	14.3
2006-10-28T03:10:54	0.001666	0.101469	0.022579	4.978289	4.173722	2.712394	14.2
2006-11-09T02:59:11	0.002004	0.090012	0.029586	4.986055	4.205401	2.662653	14.2
2006-12-03T00:36:55	0.002324	0.086552	0.024797	4.97674	4.246569	2.577651	14.1
2007-05-10T19:30:07	0.006145	0.065842	0.00417	4.759229	−4.32257	−1.99158	1.6
2007-05-26T22:40:39	0.003027	0.053444	−0.00827	3.503545	−3.19988	−1.43802	1.6
2007-06-11T23:29:38	0.078701	0.002115	0.001165	2.938634	−2.68488	−1.19415	1.6
2007-12-19T03:35:21	0.001273	0.110565	−0.01242	3.233808	−3.20682	0.46743	23.4
2008-01-03T22:05:20	0.010767	0.041161	−0.00235	4.359624	−4.30145	0.712214	23.4
2008-01-15T21:06:04	0.006164	0.051953	−0.02025	3.444221	−3.3927	0.585802	23.3
2008-01-27T19:14:48	0.003896	0.044008	−0.02575	3.443493	−3.38995	0.635914	23.3
2008-02-08T17:52:22	0.002831	0.052775	−0.01307	3.457128	−3.4028	0.633022	23.3
2008-02-20T17:52:35	0.007884	0.042135	−0.02206	3.452499	−3.39155	0.645369	23.3
2008-03-02T03:14:08	0.026511	0.034626	−0.00053	3.943226	−3.85883	0.799839	23.2
2008-03-23T10:19:53	0.026504	0.034522	−0.00222	3.944782	−3.84791	0.8712	23.1
2008-04-01T18:08:39	0.008167	0.043577	0.003094	4.490891	−4.36999	1.039286	23.1
2008-04-20T21:31:19	0.021704	0.046619	−0.00047	4.487401	−4.35227	1.093048	23.1
2008-04-30T10:44:01	0.015542	0.048642	0.005473	4.480816	−4.33729	1.120889	23
2008-05-10T00:02:39	0.017738	0.054989	0.011277	4.480402	−4.32985	1.166508	23
2008-05-17T23:03:36	0.003351	0.073496	−0.01568	3.267611	−3.15271	0.867117	23
2008-06-01T22:26:20	0.262729	0.00418	0.000162	2.731175	−2.62251	0.762803	22.9
2008-06-09T01:44:20	0.104314	0.004089	0.000072	2.730111	−2.61699	0.7777	22.9
2008-06-16T04:50:22	0.312647	0.004994	0.000417	2.713475	−2.59642	0.788437	22.9
2008-06-23T07:55:20	0.084789	0.006285	0.00024	2.711298	−2.58974	0.803144	22.9
2008-06-30T08:45:21	0.025433	0.004703	−9.3E-05	2.708354	−2.58246	0.816139	22.8
2008-07-07T09:33:50	0.290048	0.005112	0.000557	2.70665	−2.57617	0.830252	22.8
2008-07-14T10:22:44	0.043669	0.004164	0.000002	2.706991	−2.57181	0.844736	22.8
2008-07-21T11:16:19	0.027801	0.004698	0.000206	2.70942	−2.56947	0.859592	22.8
2008-07-28T12:14:29	0.108608	0.00414	−9.5E-05	2.709386	−2.56442	0.874325	22.7
2008-08-04T11:52:28	0.042153	0.037363	−0.00226	3.961838	−3.74033	1.307791	22.7
2008-08-19T05:45:47	0.033605	0.034597	0.000964	3.935132	−3.70104	1.339061	22.7
2008-08-26T14:33:19	0.052448	0.035146	−0.00086	3.973086	−3.73019	1.369217	22.7
2008-09-02T23:29:41	0.029802	0.039023	−0.00167	3.965378	−3.71699	1.379121	22.6
2008-09-10T08:20:52	0.034786	0.038829	−0.00266	3.962988	−3.70705	1.403197	22.6
2008-09-17T17:11:25	0.093825	0.035582	−0.002	3.961976	−3.69999	1.414798	22.6
2008-09-25T02:00:40	0.03787	0.039958	−0.00358	3.962396	−3.69322	1.435313	22.6
2008-10-02T10:42:23	0.025492	0.025307	0.060275	3.96604	−3.68003	1.491056	22.5
2008-10-17T03:02:02	0.03836	0.037483	−0.00232	3.955507	−3.6654	1.48515	22.5
2008-10-24T10:05:04	0.031979	0.037907	−0.00834	3.964104	−3.66659	1.50568	22.5
2008-11-08T21:15:59	0.011272	0.04793	0.00194	4.328193	−3.98136	1.697187	22.5
2008-11-16T21:07:40	0.013315	0.043278	0.004558	4.33365	−3.97651	1.721741	22.4
2008-11-24T08:41:48	0.002555	0.074195	−0.0023	5.245236	−4.79822	2.11921	22.4
2008-12-02T07:56:38	0.003672	0.068771	0.015132	5.246252	−4.786	2.148809	22.4
2008-12-09T17:46:51	0.001112	0.138274	0.025519	5.762686	−5.23485	2.4102	22.4
2008-12-17T17:09:16	0.001245	0.110506	0.02058	5.768608	−5.23432	2.424304	22.3
2009-07-26T18:29:18	0.007811	0.033516	−0.00655	4.202785	3.502527	−2.31765	9.8
2009-08-11T12:58:52	0.001512	0.12088	−0.0305	3.110577	2.600824	−1.74307	9.7

antenna. This also served to explain the difference in voltage spectral power due to dust impacts observed by the dipole and monopole antenna of Cassini RPWS (Meyer-Vernet et al., 2009, 2014). However, recent Cassini RPWS observations during ring plane crossings showed that impact *voltage signals* measured by the dipole antenna are comparable to those measured by the monopole antenna, whereas the dipole *impact rates* are about an order of magnitude lower than monopole, consistent with the projected area ratio between the antenna boom and the spacecraft body. This indicates that the dipole antenna primarily detects direct impacts on the antenna booms. In this study, we treat the dipole voltage pulses as is without multiplying by the correction factor 40 as did Ye et al. (2014).

3. Data

One of the advantages of RPWS dust detection is that this method has a much larger collecting area (the spacecraft) than that of CDA, so RPWS is expected to be able to detect much lower fluxes for a given size threshold (e.g. 1 μm). More importantly, the RPWS does not need a specific spacecraft attitude for dust detection, so it is possible for RPWS to detect dust continuously through the orbit. Unlike CDA, RPWS does not rely on any specific spacecraft attitude to carry out the measurement. For example, during the SOI, when the HGA was pointed to ram direction to shield Cassini instruments from dust hazards, CDA was not able to make any dust measurement. RPWS provided the only in-situ

measurement of dust particles during the SOI. The RPWS wideband receiver (WBR) can record the waveform of each individual dust impact, whereas the CDA High Rate Detector (HRD) can only measure the impact rate of dust particles above certain thresholds. Thus RPWS can provide a better characterization of the dust size distribution function.

That said, RPWS lacks a prelaunch calibration of the conversion from voltage measurement to particle size and its effective impact area at different attitudes. So the size and density of the dust particles measured by RPWS are subject to error. The CDA measurement of dust number density has smaller error bars than RPWS. The uncertainty of the dust number density measured by RPWS could be as large as a factor of 10. The differences between the RPWS and CDA measurements have been shown to be within this uncertainty range (Ye et al., 2014). Cross calibration with CDA measurements can help better constrain the effective area of RPWS. CDA HRD has exact size thresholds for iron grains and effective areas for its sensors, which can be used to infer the effective impact area of RPWS by comparing the impact rates measured by the two instruments.

During most of the ring plane crossings, RPWS has been scheduled to collect continuous wideband data, which we can analyze to infer the properties of the dusty rings, i.e. dust size distribution and dust number density. Fig. 1a shows a waveform of the RPWS WBR data collected during the E ring crossing on DOY 122, 2005. The receiver was operated in the 10-kHz mode and was connected to the dipole electric antenna. Dust impact waveforms typically exhibit a jump in voltage within a few tens of microseconds. The identification of dust impacts is based upon the voltage changes between two adjacent data points exceeding a certain threshold value (in this study, 4 times the voltage change value averaged over the previous 15 data points). For comparison, Fig. 1b shows the dust impact waveforms observed by the monopole antenna on DOY 248, 2005. Note that most of the voltage pulses are negative and are attributed to impacts on the spacecraft body. The fewer positive pulses are due to impacts on the electric antenna boom. The jump in voltage of each dust impact can be converted to the size (radius) of the impacting particle, assuming a spherical shape of the icy particles and water ice density of 920 kg/m^3 (Ye et al., 2014).

A Fourier transform of the dust impact waveforms yields a power law spectrum with a hinge at a few kHz. The slope of the power law is −4 above the hinge frequency and −2 below. Aubier et al. (1983) modeled the waveform of the dust impacts and showed that the power law spectrum due to the dust impacts can be used to infer the size and number density of the impacting particles (Meyer-Vernet et al., 1996, 2009; Schippers et al., 2014). Based on the model, the hinge frequency is controlled by the rise time of the impact pulse. The WBR spectrogram during the E ring crossing (at Enceladus' orbit) on DOY 122, 2005 is shown in Fig. 2, where intense dust impact signals appear as vertical spikes. The most intense signals due to dust impacts are approximately coincident with the crossing of ring plane by the spacecraft. It is noticed that there is an enhancement of dust impact signals around 22:05, away from the ring plane, corresponding to a local dust density spike. Examination of the waveform plots confirmed that dust impacts were observed during this time period. Similar enhancements of dust impact rates off the ring plane were also observed during the ring plane crossing (at 4.36 Rs) on DOY 003, 2008 around 22:45 and 23:52, when Cassini was at around −6° and −14° latitude. The origin of these high latitude dust particles is still unclear. Note that the Voyager 2 plasma wave instrument also observed increases in root mean square dust impact signals off the ring plane (1000–3000 km south) during the ring plane crossing just exterior to the G ring (Tsintikidis et al., 1994).

Because the WBR can detect individual dust impacts and measure their sizes, the data can be used to characterize the size distribution of the dust particles. The sizes of all dust impacts detected within a time window (e.g. 1 min) are sorted into equal size bins of a histogram as shown in Fig. 3. The result shows a differential power law size distribution within the sensitive size range of each gain, which is an amplifier set based on waveform amplitudes to maximize the use of the A/D dynamic range while minimizing clipping (exceeding the range of the A/D converter) (Gurnett et al., 2004). The gain is determined by onboard software once every few seconds but is applied between waveform snapshots (private communication, Donald Kirchner). With the help of the automatic gain control, the dynamic range of the WBR is greatly expanded, resulting in the instrument's sensitivity to a wide size range of particles (submicron to 10 μm). Although the sensitive size range at one particular time is narrow, the changing gain helps us to peek into different sections of the general size distribution, which all resemble a power law function. The slopes measured within each gain are also similar, supporting a wide power law size distribution. The slopes of the size distributions measured with the WBR gain set at 30 and 40 dB are −4.2 and −3.5 respectively, which are consistent with the size distribution slope derived from fitting the impacts rates with different size thresholds.

The dust density is given by $n = R/AU$, where R is the impact rate, A is the effective impact area of the spacecraft and U is the ram velocity between the spacecraft and the dust particles. We have assumed the dust particles of these sizes move in a circular Keplerian orbit around Saturn. However, the orbits of the E ring particles are likely eccentric, so this assumption may not strictly hold, which could introduce (small) systematic errors in the estimates of the particle size and density in the inner and outer parts of the E ring. For this study, the impact rate R is computed as the number of impacts divided by the total sampling time within a moving time window (25 s). The instrument detection threshold is dependent on the gain of the receiver, which is subject to change during the ring plane crossing. This is because the automatic gain control of the receiver responds to the total signal level of the band. When more and more impacts are detected, this level increases, eventually requiring the gain to be decreased. As a result, the smallest impact signals (now weaker than before the gain change) will become too small to be detected, effectively increasing the detection threshold of the instrument. So we use the observed rates to estimate the total number of impacts by grains with radii greater than 1 μm, assuming that the power law distribution extends down to at least 1 μm. The fitted slope of the size distribution often has large variations (e.g. −2 to −7) or is not available when the impact rates are low. So we apply a size slope −4 to all data (the fitted size slopes during the ring plane crossings range from −3 to −5), which could overestimate or underestimate the dust density where the actual size slope is different from −4. During the ring plane crossings, the detection thresholds of the RPWS instrument were close to 1 μm (within a factor of three), so the uncertainty of the dust density due to the scaling is within a factor of three (assuming the size slope is off by one).

In Fig. 4, we plot the dust density versus vertical distance from the ring plane, for ring plane crossings at four different radial distances, representing the region around the G ring (panel a), inner E ring (panel b), Enceladus' orbit (panel c), and outer E ring (panel d). The dust densities are calculated from the number of impacts counted within 25-second moving windows. For the ring plane crossing at 5.7 R_S (panel d), the data are quite noisy compared to the other ring plane crossings. This is likely due to two reasons. First, when the density is low, the number of impacts detected in each sampling window is small, so the variance of the impact rate is large compared to the average. Second, low frequency plasma waves often observed in this region interfere with the dust detection algorithm (the oscillating electric field of the plasma waves causes rapid changes of voltage, which could be

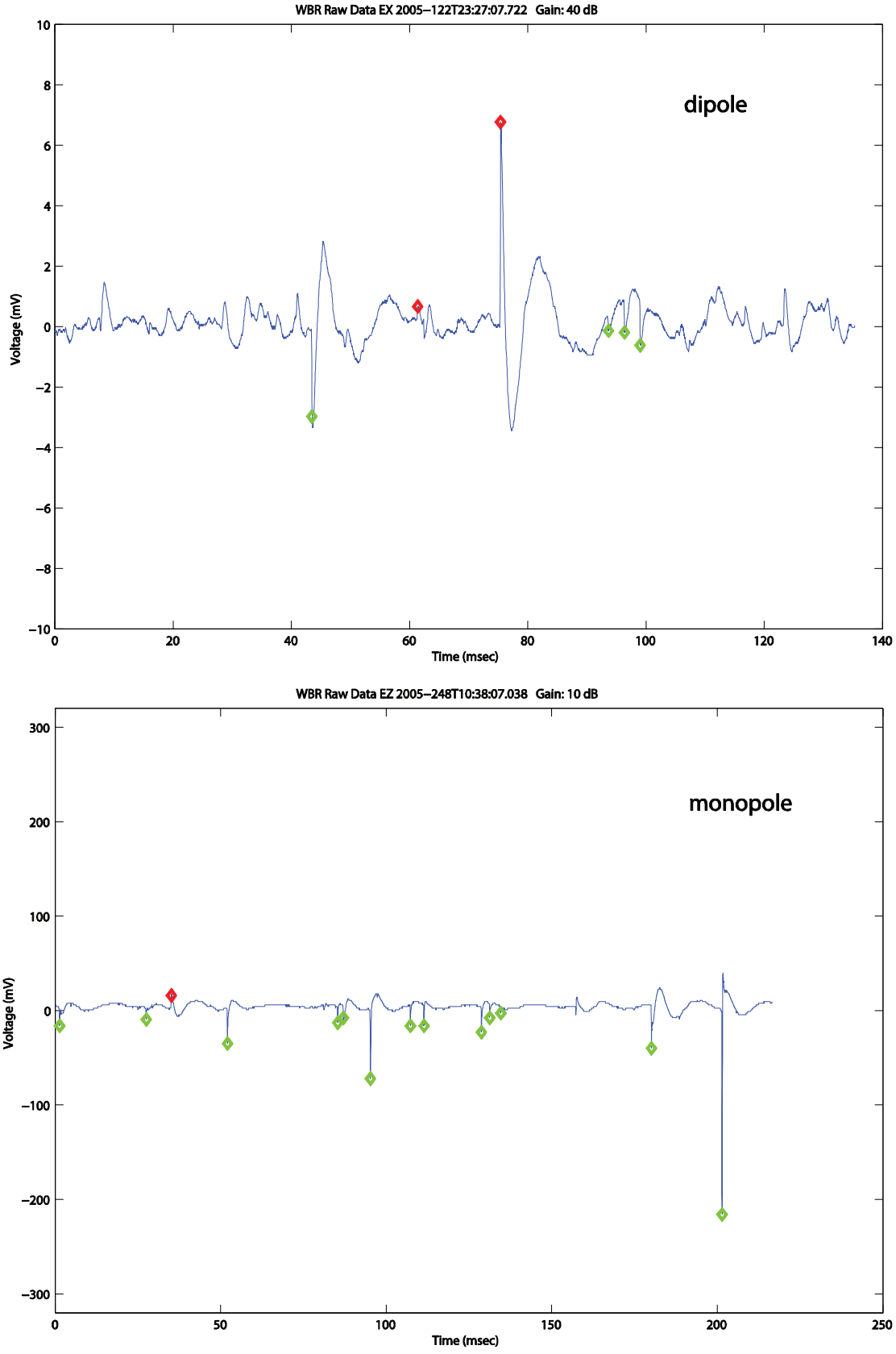

Fig. 1. Waveform snapshot of the RPWS wideband receiver data collected during the E ring crossing on DOY 122, 2005 (top) and near the G ring on DOY 248, 2005 (bottom). The receiver was in 10-kHz mode and connected to the dipole and monopole antenna, respectively. The identified dust impacts are marked by diamonds at the peak of each voltage impulse.

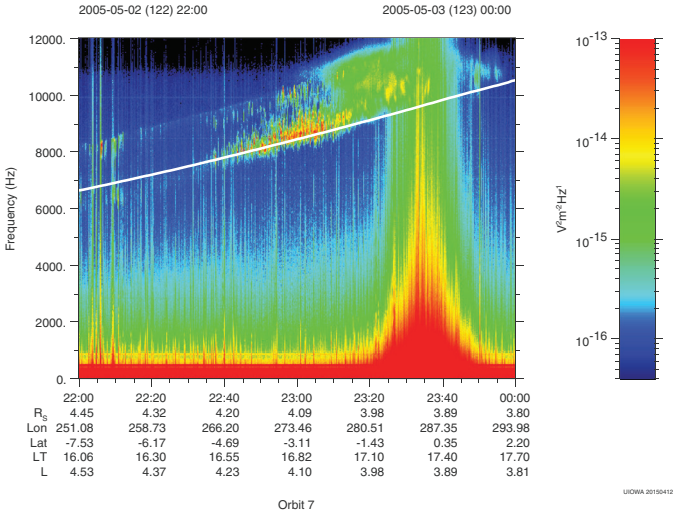

Fig. 2. The WBR spectrogram during the E ring crossing on DOY 122, 2005, where intense dust impact signals appear as vertical spikes. The white line is the local electron cyclotron frequency calculated from the magnetic field measured by MAG.

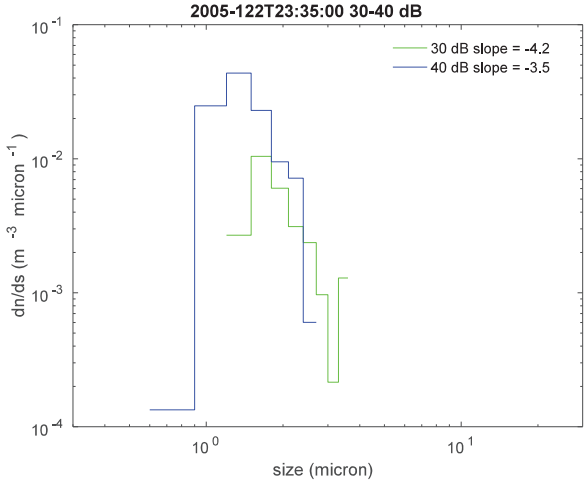

Fig. 3. Size distribution of the dust particles detected during the E ring crossing on DOY 122, 2005. For two different receiver gains, the sizes of all dust impacts detected are sorted into equal size bins of a histogram, which shows a power law size distribution within the sensitive size range (1–3 μ). The lack of particles smaller than 1 μm is due to the instrument cut-off in sensitivity at around 1 μm. The sensitivity threshold is dependent on both the impact velocity and the gain of the receiver. (For interpretation of the references to color in this figure legend, the reader is referred to the web version of this article.)

mistaken as dust impacts by the dust identification algorithm). Filtering out the interference of the plasma waves increases the size threshold for dust identification, which also reduces the number of dust impacts detected in each sampling window.

For each ring plane crossing, the dust density is fitted with a Lorentzian function (plotted in red). The function form is given by

$$n = \frac{n_0 w^2}{(z - z_0)^2 + w^2} \tag{4}$$

Where n_0 is the peak density and z_0 is the vertical offset of the peak density. From this model fitting, the peak density and half width at half maximum (w) of each density profile can be determined. It is noted that the vertical thickness of the dusty rings is a function of the radial distance from Saturn. The ring's vertical thickness around the G ring is about one tenth of the thickness at the Enceladus orbit. The thickness of the E ring grows with the distance from Enceladus' orbit. More interestingly, the peak density location of the E ring shifts from south to north of Saturn's equatorial plane with increasing radial distance from the planet. Also, local density minima are observed at ring plane crossings around Enceladus' orbit (panel c). Most of these features were also observed by the CDA (Kempf et al., 2008) and ISS instruments onboard Cassini (Hedman et al., 2012). The CDA HRD could not resolve the density dips at ring plane crossings around the Enceladus orbit.

Fig. 5 shows the radial dust density profile derived from the WBR data collected on DOY 266, 2005. This equatorial crossing of the E ring was also analyzed by Kurth et al. (2006). Here we apply the dust identification algorithm used by Ye et al. (2014) on the same data and redo the power law fit. It is shown that the radial density profile of the E ring can be represented by power laws interior and exterior to the Enceladus orbit $n = n_0(\rho/3.95)^p$, with the power law index p = 17 and -9 respectively. Note that Showalter et al. (1991) found the power law indices to be 15 and −7 based on optical observations of the E ring. For comparison, the corresponding power law indices determined by Kurth et al. (2006) are 24.8 and -8. The difference between this study and Kurth et al. (2006) is likely due to the difference in sensitivity of the two dust detection algorithms. The density of dust particles above the 1 μm size threshold shown in Fig. 5 are estimated from the detected impact rates at all gains (for particles larger than the detection threshold of the WBR, which changes with gain) based on the assumption of a power law distribution with index −4, whereas Kurth et al. (2006) derived their power law fit based on impact rates detected at 30 dB gain. It is worth pointing out that during the equatorial crossing of the E ring, the spacecraft had vertical offset from the ring plane, which means the densities measured might not be peak densities. Also, as shown earlier, the peak density locations of the E ring have vertical offsets from the equatorial plane interior and exterior to the Enceladus orbit. All these factors render the measurement of radial density profile of the E ring by a single equatorial crossing inaccurate.

In order to better resolve the density profile of the E ring, we analyzed all high inclination ($v_z/v > 0.3$, v and v_z are velocity and its z component of the spacecraft relative to Saturn) orbits that cut through the E ring between the SOI and equinox. For each high inclination crossing of the E ring, we plot the dust density versus the vertical offset from the equatorial plane and fit the vertical density profile to a Lorentzian function. From each fit, we obtain the peak density n_0, radial distance corresponding to the peak location r_{max}, vertical thickness w (half width at half maximum) and the vertical offset of the peak location z_0. The fitted parameters and spacecraft locations of all the ring plane crossings analyzed in this study are listed in Table 1. These RPWS results can be compared to observations by other instruments onboard Cassini, e.g. CDA and ISS.

In Fig. 6, we plot the peak densities of the high inclination ring plane crossings versus the radial distances of the peak density locations in a semi-log axis. There are basically two regions with relatively high dust density, the region around the G ring interior to 3 R_S and the region around Enceladus' orbit at 3.95 R_S. The highest densities are measured during the Enceladus flybys (excluded from this study). The dust densities interior and exterior to Enceladus' orbit fall off roughly as power law functions as indicated by the straight line fits (red) in the semi-log plot. The power law fit of the radial density profile of the E ring is expressed as $n = n_0(\rho/3.95)^p$, where $n_0 = 0.035$ m^{-3} is the peak dust density (>1 μm) at Enceladus' orbit, ρ is the radial distance in R_S and $p = 16 \pm 2$ and -10 ± 1.6, interior and exterior to Enceladus' orbit. The uncertainty interval for p is based on 95% confidence level. For comparison, CDA measured a peak density (>0.9 μm) of 0.05/m^3 at the Enceladus orbit (Kempf et al., 2008). The scatter of the density data around the fitted red curves is probably due to the local time dependence of the ring's density profile as observed by ISS (Hedman et al., 2012).

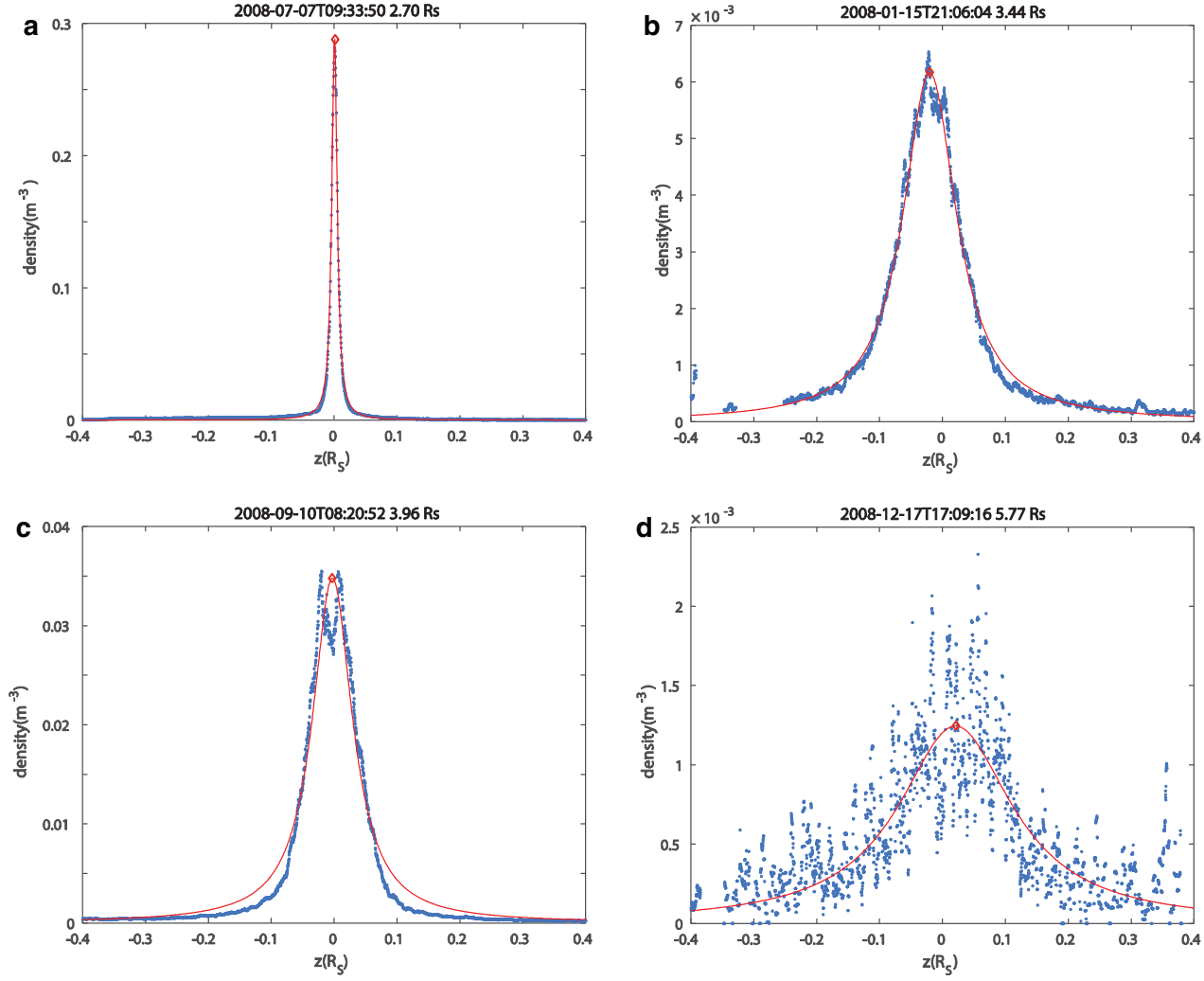

Fig. 4. Scaled dust density (>1 μm) versus vertical distance from the ring plane for selected ring plane crossings. The time and radial distances of the ring plane crossings are shown on top of the panels. (a) The region interior to the G ring; (b) E ring interior to Enceladus orbit; (c) E ring core; (d) E ring exterior to Enceladus orbit. The red curves are Lorentzian function fits to the densities and the red diamonds mark the density peaks. The density profiles are calculated based on impacts counted within a 25-second moving window. (For interpretation of the references to color in this figure legend, the reader is referred to the web version of this article.)

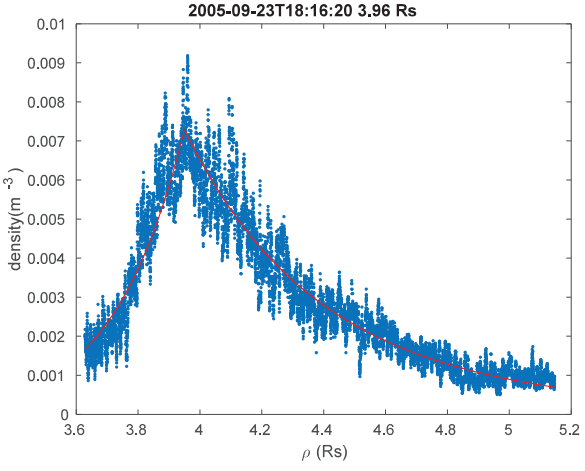

Fig. 5. Radial dust density profile derived from WBR data collected on DOY 266, 2005. The red lines are the power law fits of dust densities interior and exterior to the Enceladus orbit, $n = n_0(\rho/3.95)^p$, with $n_0 = 0.007$ and p = 17 and −9, respectively. For comparison, see Fig. 1 of Showalter et al. (1991), where the inner and outer exponents are 15 and −7, respectively. (For interpretation of the references to color in this figure legend, the reader is referred to the web version of this article.)

In Fig. 7, we plot the vertical thickness (w, half width at half maximum) of the dusty rings as a function of radial distance. It is noticed that the thickness parameter w of the G ring is below 0.005 R_S. The thickness of the E ring has a minimum (w~0.033 R_S) at Enceladus' orbit and increases with the distance from Enceladus' orbit, which is consistent with Enceladus being the source of the E ring particles (Haff et al., 1983; Pang et al., 1984; Showalter et al., 1991). The thickness (w in R_S) of the E ring can be roughly represented by functions of the radial distance ρ as $w = 0.034 - 0.066(\rho - 3.95)$ and $w = 0.032 + 0.044(\rho - 3.95)$ for regions interior ($3 < \rho < 3.95\,R_S$) and exterior ($3.95 < \rho < 6\,R_S$) to Enceladus' orbit. The thickness (full width at half maximum, FWHM) of the E ring measured by CDA at Enceladus' orbit is ~4300 km, comparable to the RPWS observation (~4000 km), but the CDA measured E ring thickness at the Mimas orbit (~5000 km) is significantly smaller than the value measured by RPWS (~10,000 km) during the same ring plane crossing (Kempf et al., 2008). The RPWS value is more consistent with the FWHM at the Mimas orbit derived from the optical images (de Pater et al., 2004). While the overall trends in the ring's thickness are consistent with previous measurements and models, it is difficult for RPWS in-situ observations to reveal the variation of ring thickness with local time (as shown in Fig. 6 of Hedman et al. (2012)), because the ring plane

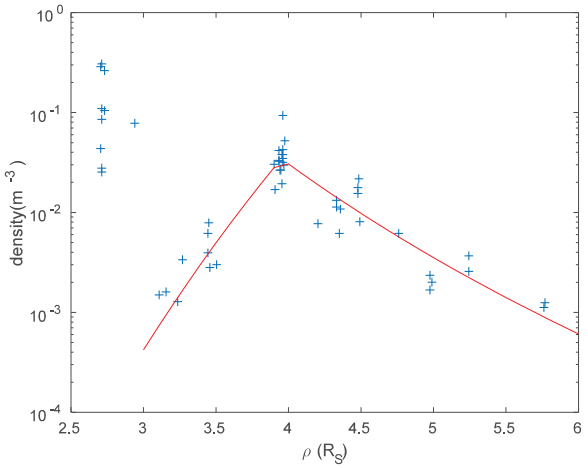

Fig. 6. Peak densities of the high inclination ring plane crossings versus the radial distances of the peak density locations in a semi-log plot. The red lines are the power law fits of the radial density profile of the E ring, expressed as $n = n_0(\rho/3.95)^p$, where $n_0 = 0.035\ m^{-3}$ is the peak dust density (>1 μm) at Enceladus orbit, ρ is the radial distance in R_S and $p = 16 \pm 2$ or -10 ± 1.6 interior or exterior to Enceladus orbit. Note the scatter of the density data around the fitted red curves. The uncertainty interval for p is based on 95% confidence level. The density measurements around 2.7 and 2.9 R_S (vicinity of the G ring) are comparable to or higher than those at the E ring core. (For interpretation of the references to color in this figure legend, the reader is referred to the web version of this article.)

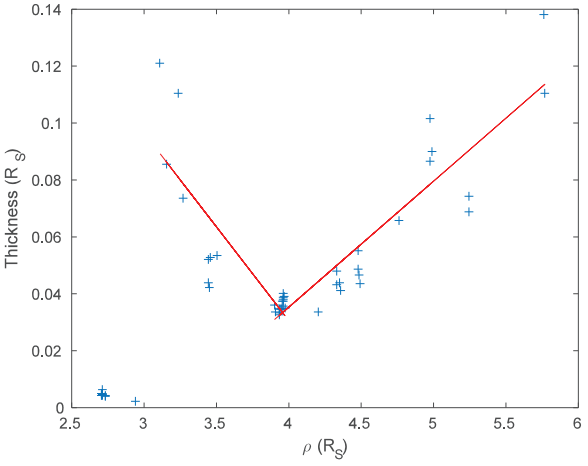

Fig. 7. Vertical thickness (w, half width half max) of the dusty rings as a function of radial distance. The fitted functions are $w = 0.034 - 0.066(\rho - 3.95)$ and $w = 0.032 + 0.044(\rho - 3.95)$ interior and exterior to the Enceladus orbit. The scatter of the data around the fitted lines are probably due to the local time dependence of the E ring thickness (Hedman et al., 2012). Note that the vertical thickness around the G ring is below 0.005 R_S. (For interpretation of the references to color in this figure legend, the reader is referred to the web version of this article.)

crossings were not evenly distributed in local time and radial distance space.

Fig. 8 shows the vertical offsets of dust density peak locations (z_0) as a function of the radial distance ρ (in R_S). The dust density peaks measured around the G ring remain very close to the equatorial plane, while the E ring peak locations shift from south to north of the equatorial plane as the radial distance from Saturn increases, similar to that observed by ISS (Hedman et al., 2012). For most of the ring plane crossings near Enceladus' orbit, the peak locations are slightly south of the equatorial plane, which cannot be explained by the south polar jets because the material jetted southward from Enceladus goes equally far northward half an orbit later. The vertical offsets of the density peaks can be roughly represented by the function $z_0 = -0.005 + 0.018(\rho - 3.95)$, where

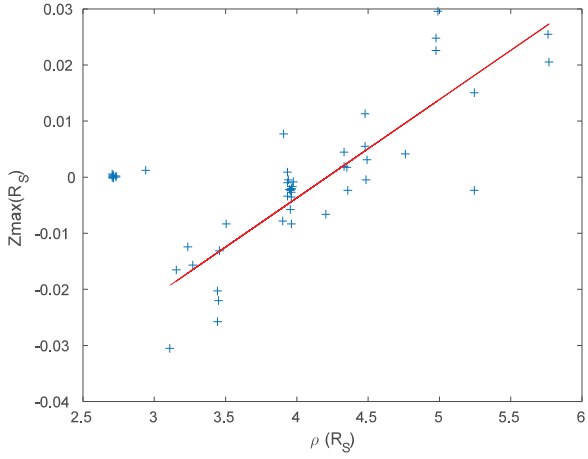

Fig. 8. Vertical offsets of dust density peak locations (z_0) as a function of the radial distance. The fitted function (red line) is $z_0 = 0.018(\rho - 3.95) - 0.005$. (For interpretation of the references to color in this figure legend, the reader is referred to the web version of this article.)

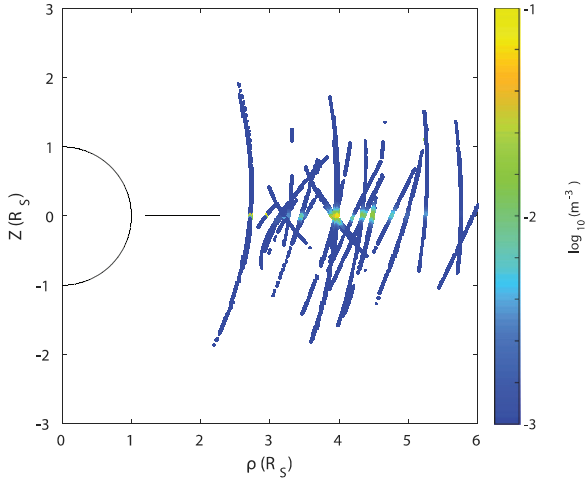

Fig. 9. Dust density (>1 μm) profiles measured during all high inclination RPXs (listed in Table 1) between DOY 122, 2005 and DOY 223, 2009 in polar coordinates. The base ten logarithm of dust densities are color coded so that yellow represents $0.1/m^3$ and blue represents $0.001/m^3$.

$3 < \rho < 6\,Rs$. The southward displacement of the E ring peak at Mimas measured by the RPWS (~1000 km) is consistent with the CDA measurement (~1200 km) (Kempf et al., 2008).

Fig. 9 shows all the dust density profiles measured during the high inclination crossings ($v_z/v > 0.3$) between the SOI and equinox in cylindrical coordinates. The size threshold for the dust density calculation is 1 μm. One can notice from this plot that the ring thickness of the region around the G ring is much smaller than that of the E ring. The dust density clearly peaks at the orbit of Enceladus. However, the variation of the thickness and the vertical offset of the dust density peak of the E ring are not very obvious due to the scale of the plot.

4. Discussion

Cassini RPWS can directly measure dust particles in Saturn's dusty rings via the impact signals induced on the electric antenna. This method can detect more dust impacts per unit time (compared to CDA) for a given size threshold (e.g. 1 μm) due to the relatively large effective area and thus is more sensitive to low dust fluxes. Because the generation of the impact signal is not reliant on the spacecraft attitude, the measurement of dust particles

is available whenever the WBR is scheduled to collect data. The RPWS measurements of dust particles have been calibrated with CDA HRD data at three different locations, the E ring, G ring and the Enceladus plume (Kurth et al., 2006; Ye et al., 2014). Continuous waveform measurement by the WBR during most of the ring plane crossings provides the opportunity to compare the RPWS measured dust properties to those observed by optical instruments like ISS.

Photometric modeling trials based on various assumptions of the particle size distribution lead to the conclusion that only a narrow size distribution fit the E ring observation (Showalter et al., 1991). Cassini VIMS observations of the Enceladus plume indicates that most of the larger size (>3 μm) dust particles are ejected from the south pole of Enceladus at a lower velocity and thus cannot escape the gravity of the Moon (Hedman et al., 2009). Ingersoll and Eward (2011) deduced that the best fit size distribution of the particles in the Enceladus plume, based on modeling of the ISS observations of the plume, is basically a power law with an exponent between −6 and −12. We compare the remote sensing results to the in-situ measurements by CDA and RPWS in the corresponding regions. During the high inclination orbits in 2008, when the impact speed was close to 20 km/s, RPWS was sensitive to submicron particles, because the charge yield is proportional to impact speed to the power 4.6. RPWS observed dust particles with sizes close to 10 μm during the Enceladus plume crossings. The observation is consistent with a wide size range with steep power law distribution. In particular, RPWS measurements clearly showed that the differential particle size distribution in the E ring is characterized as a power law (size slope ∼ −4) (Ye et al., 2014), which is consistent with CDA observations (size slope ranges from −4.2 to −5.4) (Kempf et al., 2008). The difference between all these measurements could not be reconciled by a size distribution of which the power law index changes with the size, because RPWS is sensitive to a wide size range (submicron to 10 μm, with the help of automatic gain control) which contains the size range that optical instruments are sensitive to. More work is needed to understand the potential discrepancies between the different measurements.

Horanyi et al. (1992) proposed a dynamic filtering process which would determine the size distribution of the E ring particles as a function of location. The CDA measurements showed that the size distribution of freshly injected plume particles agrees with the size distribution of the background E ring particles (Kempf et al., 2008). RPWS also did not observe significant change in the size distribution slope during the ring plane crossings at Enceladus' orbit and high inclination Enceladus flybys. The size distribution slopes fitted from RPWS observations at different radial distances (3–6 R_S) seem to match within uncertainties, which are usually high on the edges of the E ring due to lower dust impact rates. So, it's hard to draw any conclusion on the spatial dependence of the size distribution slope based on RPWS data. Although, theoretically, dust dynamics is a function of grain size, other processes such as plasma drag might smear things out. The dynamic filtering process mainly involves eccentricity changes rather than semi-major axis changes, so one would not necessarily expect the size distribution to change radically in the vicinity of Enceladus' orbit.

Note there is uncertainty in the size of the particles inferred from RPWS measurements due to the uncertainty in the charge yield and in the charge-antenna coupling process. The charge yield per unit mass of dust particle used in this study is about 5 times lower (for 10 km/s impact speed) than that used in Ye et al. (2014). And there would be significant difference in the charge antenna coupling efficiency whether the dust impacts on the spacecraft body or directly on the antenna boom. See the difference in the particle sizes derived by Gurnett et al. (1983), Tsintikidis et al. (1994), Tsintikidis et al. (1995), where different assumptions on the coupling mechanism have been made. The particle sizes derived in this study (a few microns) are consistent with the Gurnett et al. (1983) result, whereas the particle sizes derived in Ye et al. (2014) are more consistent with Tsintikidis et al. (1994, 1995) results, because these studies assumed ∼40 times lower charge-antenna coupling efficiency for the dipole mode compared to the monopole mode. As a result, the derived mass of the dust particles could be off by a couple of orders of magnitude. However, during a particular ring plane crossing, the relative sizes of the particles detected by RPWS during one orbit are not affected by the uncertainty because the uncertainty associated with each voltage to mass conversion should be the same. So the shape of the distribution function, e.g. the power law index, is pretty accurately determined. The size distribution function can be compared with the predictions of various physical models for the origin and acceleration of the dust particles (e.g. Schmidt et al., 2008). The RPWS in-situ measurements can provide constraints on parameters to be used in the future modeling studies based on remote sensing data.

The RPWS measurements of dust density in the flight path is based on the recorded impact rates and the estimated effective impact area of the spacecraft (Wang et al., 2006). Changing the orientation of the spacecraft will change the effective impact area and maybe the charge yield constant. For the monopole mode, the spacecraft body is the main impact surface, the cross sectional area of which will change with the orientation of the spacecraft. The material of the spacecraft surface exposed to the ram direction will affect the charge yield of the impacts. For example, the same dust particle impacting at the same speed would yield different amount of charge on the high gain antenna and the thermal blanket, which are covered with different materials. For the dipole measurement, RPWS primarily detects impacts on the antenna booms, the effective area of which changes with the spacecraft attitude. So for the ring plane crossing data in this study (collected in the dipole mode), we used the projected area of the RPWS electric antenna boom (∼0.4 m^2) as the effective impact area. For comparison, Ye et al. (2014) used 1.5 m^2, based on the assumption that the dipole antenna detects impacts on the spacecraft body. Combined with the smaller charge yield, the dust density derived in this study is about 5–10 times lower than the computation in Ye et al. (2014) would have obtained. Although the RPWS dust density measurement has one order of magnitude uncertainty, the factor needed to correct the measurement to the real value should be a constant value. So the measured density profiles are similar to the real density profiles and provide accurate peak locations and thickness of the dusty rings, as shown in the comparison to the observations by ISS (Hedman et al., 2012).

When fitting the vertical density profiles with Lorentzian functions, the best-fit parameters plotted versus the radial distance from Saturn (Figs. 6–8) resemble the corresponding plots based on the ISS data (Fig. 3 of Hedman et al. (2012)). First of all, both instruments observed density peaks at the G ring and Enceladus' orbit, consistent with G ring moonlets and Enceladus being the source of dust particles. Second, both instruments observed local density minima at the ring plane near Enceladus' orbit. The density minima at the ring plane also shows up in many numerical simulations (e.g. Juhász et al., 2007; Horanyi et al., 2008; Kempf et al., 2010). The non-zero speeds at which the particles are launched from Enceladus' south pole and the moon's gravity provides the vertical velocity of the dust particles, reducing the local particle density near the ring plane over a range comparable in size to Enceladus' Hill sphere (Hedman et al., 2012). Third, the average density peak offset from the equatorial plane shifts from about −0.03 R_S to about 0.03 R_S as the radial distance from Saturn increases from 3 R_S to 6 R_S. This vertical warp of the E ring is also observed by ISS, where the E ring's peak brightness density shifts from 1000–2000 km southwards of Saturn's equatorial plane to 1000+ km northwards between the orbits of Mimas and Tethys

(Hedman et al., 2012). This E ring warp is due to the locking of the pericenters and apocenters of the dust orbits out of the equatorial plane by the vertical forces from solar radiation pressure and the planet's aligned quadrupolar field (Hamilton 1993). It was also predicted that the E ring warp would vary with time due to the seasonal change of radiation pressure normal direction relative to the ring plane. Voyager 1 observations during the ring plane crossing near Dione showed that the E ring peak was centered about 2500 km below the equatorial plane (Tsintikidis et al., 1995). The measurement was taken on November 13, 1980, about 8 months after the vernal equinox of Saturn (March 3), when the solar radiation came from north of the ring plane. So the Voyager 1 observation seems to be consistent with the seasonal control of the warping of the E ring. Cassini E ring image data also showed that the warping direction has reversed after equinox (private communication, M. M. Hedman). Fourth, the vertical thickness (w, half width at half maximum) of the E ring measured by RPWS is at its minimum ~0.033 R_S at the Enceladus orbit and increases linearly with the distance from Enceladus orbit, reaching about 0.1 R_S and 0.12 R_S at 3 R_S and 6 R_S radial distances, respectively. This result is also consistent with the modeling results and previous observations (Horanyi et al., 1992; Nicholson et al., 1996; de Pater et al., 2004; Hedman et al., 2012). Note that RPWS observed a larger (factor of ~2) thickness of the E ring at the Mimas orbit than CDA, and that CDA did not resolve the density dip at the ring plane near Enceladus' orbit.

Ingersoll and Ewald (2011) estimated the total mass of particles in Enceladus' plume ($(1.45 \pm 0.5) \times 10^5$ kg) and the E ring ($(12 \pm 5.5) \times 10^8$ kg) and deduced the lifetime of the dust particles in E ring to be ~8 years. We integrated the dust density (>1 μm) measured by RPWS over the dense part of the E ring (3–6 R_S radial distance, −1 to 1 R_S vertical offset from the equatorial plane) and estimated the total mass to be 2×10^8 kg. The uncertainty of the total mass due to the uncertainty of the power law size slope is estimated to be a factor of 2. The estimated mass production rate of the Enceladus plume is 51 ± 18 kg/s by Ingersoll and Ewald (2011), 15–65 kg/s by Dong et al. (2015), and 5 kg/s by Schmidt et al. (2008). Note that Dong et al. (2015) estimated the total (nanometer to 50 μm in size) mass production rate based on the micron dust density derived using the method of Ye et al. (2014), which yielded densities about 10 times larger than this study. If 10% of these particles can leave the Hill sphere of Enceladus, the E ring is replenished at 10% of the rates quoted above. The calculated lifetime of the particles in the E ring would range from 1 to 12 years. For comparison, Hamilton and Burns (1994) analytically derived the lifetime of the particles to be 20 years.

5. Conclusion

In this study, we have shown characteristics of dust particles derived from Cassini RPWS observations during the crossings of Saturn's dusty rings. Because the voltage signals induced by the dust impacts on the electric antenna are proportional to the particle sizes, we are able to derive the particle size distribution based on the RPWS data. The size distribution can be represented by a power law function of the particle radius with an exponent close to −4. The dust density profiles of the E ring are derived based on the impact rates measured by the RPWS wideband receiver. We have analyzed the ring plane crossing data within 6 R_S of Saturn's center collected between SOI and equinox (85 ring plane crossings, of which 53 high inclination crossings are listed in Table 1, and there will be 97 more ring plane crossings between equinox and the planned end of Cassini mission in 2017). The region around the G ring is found to be a very thin layer of dust particles with no observable vertical offset from the ring plane. A density model of the E ring is constructed based on fitting the density measurements with Lorentzian functions for the vertical structure and power law functions for the radial structure. It is found that the thickness of the E ring has a minimum at the Enceladus orbit and increases with the distance away from Enceladus' orbit. The vertical offset of the peak density of the E ring also shifts from ~0.3 R_S south of the ring plane at 3 R_S to ~0.3 R_S north of the ring plane at 6 R_S. There is also a local density dip at the equatorial plane in the vertical density profiles observed near Enceladus' orbit. All these features are consistent with the remote sensing measurement of the E ring by ISS (Hedman et al., 2012). The RPWS in-situ measurements of dusty rings provide valuable constraints for the dust properties of the E ring and Enceladus' plume, which are important inputs for future modeling studies. The RPWS measurement of the dust size distribution slope is also important for the evaluation of the spacecraft safety during the upcoming F ring and proximal orbits of Cassini.

Acknowledgments

This research was supported by NASA through contract 1415150 with the Jet Propulsion Laboratory. The data used in this study are available through the Planetary Data System or from the authors. We thank Chris Piker for accelerating the access to the wideband receiver data, without which this study would not be possible.

References

Aubier, M.G., Meyer-Vernet, N., Pedersen, B.M., 1983. Shot noise from grain and particle impacts in Saturn's ring plane. Geophys. Res. Lett. 10, 5–8.
Collette, A., Grün, E., Malaspina, D., et al., 2014. Micrometeoroid impact charge yield for common spacecraft materials. J. Geophys. Res.: Space Phys. 119 (8), 6019–6026.
Collette, A., Meyer, G., Malaspina, D., et al., 2015. Laboratory investigation of antenna signals from dust impacts on spacecraft. J. Geophys. Res.: Space Phys 120 (7), 5298–5305.
de Pater, I., Martin, S.C., Showalter, M.R., 2004. Keck near-infrared observations of Saturn's E and G rings during Earth's ring plane crossing in August 1995. Icarus 172 (2), 446–454. doi:10.1016/j.icarus.2004.07.012.
Dong, Y., Hill, T.W., Ye, S.-Y., 2015. Characteristics of ice grains in the Enceladus plume from Cassini observations. J. Geophys. Res. 120 (2), 915–937. doi:10.1002/2014JA020288.
Feibelman, W.A., 1967. Concerning the "D" ring of Saturn. Nature 214, 793–794. doi:10.1038/214793a0, (20 May 1967).
AGU Monograph 103 Gurnett, D.A., 1998. Principles of space plasma wave instrument design. In: Pfaff, R., Borovsky, J., Young, D. (Eds.), Measurement Techniques for Space Plasmas. American Geophysical Union, Washington, DC, pp. 121–136.
Gurnett, D.A., Grün, E., Gallagher, D., et al., 1983. Micron-sized particles detected near Saturn by the Voyager plasma wave instrument. Icarus 53, 236–254.
Gurnett, D.A., Kurth, W.S., Scarf, F.L., et al., 1987. Micron-sized particle impacts detected near Uranus by the Voyager 2 plasma wave instrument. J. Geophys. Res. 92, 14959–14968.
Gurnett, D.A., Kurth, W.S., Kirchner, D.L., et al., 2004. The Cassini radio and plasma wave science investigation. Space Sci. Rev. 114, 395–463.
Haff, P.K., Eviatar, A., Siscoe, G.L., 1983. Ring and plasma: The enigmae of Enceladus. Icarus 56 (3), 426–438.
Hamilton, D.P., 1993. Motion of dust in a planetary magnetosphere: Orbit-averaged equations for oblateness, electromagnetic, and radiation forces with application to Saturn's E ring. Icarus 101 (2), 244–264.
Hamilton, D.P., Burns, J.A., 1994. Origin of Saturn's E ring: Self-sustained, naturally. Science-AAAS-Weekly Paper Edition-including Guide to Scientific Information 264 (5158), 550–552.
Hamilton, D.P., Skrutskie, M.F., Verbiscer, A.J., et al., 2015. Small particles dominate Saturn/'s Phoebe ring to surprisingly large distances. Nature 522 (7555), 185–187.
Hedman, M.M., Burns, J.A., Tiscareno, M.S., et al., 2007. The source of Saturn's G Ring. Science 317 (5838), 653–656. doi:10.1126/science.1143964.
Hedman, M.M., Nicholson, P.D., Showalter, M.R., et al., 2009. Spectral observations of the Enceladus plume with Cassini-VIMS. Astrophys. J. 693 (2), 1749–1762. doi:10.1088/0004-637x/693/2/1749.
Hedman, M.M., Burns, J.A., Hamilton, D.P., et al., 2012. The three-dimensional structure of Saturn's E ring. Icarus 217 (1), 322–338. doi:10.1016/j.icarus.2011.11.006.
Horanyi, M., Burns, J.A., Hamilton, D.P., 1992. The dynamics of Saturns E ring particles. Icarus 97 (2), 248–259. doi:10.1016/0019-1035(92)90131-p.
Horányi, M., 1996. Charged dust dynamics in the Solar System. Annu. Rev. Astron. Astrophys. 34 (1), 383–418.
Horányi, M., Juhász, A., Morfill, G.E., 2008. Large-scale structure of Saturn's E ring. Geophys. Res. Lett. 35 (4), 5. doi:10.1029/2007gl032726.

Ingersoll, A.P., Ewald, S.P., 2011. Total particulate mass in Enceladus plumes and mass of Saturn's E ring inferred from Cassini ISS images. Icarus 216 (2), 492–506. doi:10.1016/j.icarus.2011.09.018.
Juhász, A., Horányi, M., Morfill, G.E., 2007. Signatures of Enceladus in Saturn's E ring. Geophys. Res. Lett. 34 (9). doi:10.1029/2006GL029120.
Kempf, S., Beckmann, U., Klostermeyer, G., et al., 2008. The E ring in the vicinity of Enceladus I. Spatial distribution and properties of the ring particles. Icarus 193, 420–437.
Kempf, S., Beckmann, U., Schmidt, J., 2010. How the Enceladus dust plume feeds Saturn's E ring. Icarus 206, 446–457.
Kempf. S., M. Horányi, A. Juhász, et al., (2012), The 3-dimensional structure of Saturn's E ring inferred from Cassini CDA observations, Vol. 7 EPSC2012-701.
Kurth, W.S., Averkamp, T.F., Gurnett, D.A., et al., 2006. Cassini RPWS observations of dust in Saturn's E ring. Planet. Space Sci. 54, 988–998.
Meyer-Vernet, N., 1985. Comet Giacobini-Zinner diagnosis from radio measurements. Adv. Space Res. 5, 37–46.
Meyer-Vernet, N., Lecacheux, A., Pedersen, B.M., 1996. Constraints on Saturn's E ring from the Voyager 1 radio astronomy instrument. Icarus 123, 113–129.
Meyer-Vernet, N., Lecacheux, A., Kaiser, M.L., et al., 2009. Detecting nanoparticles at the radio frequencies: Jovian dust stream impacts on Cassini/RPWS. Geophys. Res. Lett. 36, 3103.
Meyer-Vernet, N., Moncuquet, M., Issautier, K., et al., 2014. The importance of monopole antennas for dust observations: why Wind/WAVES does not detect nanodust. Geophys. Res. Lett. 41 (8), 2716–2720.
Nicholson, P.D., Showalter, M.R., Dones, L., 1996. Observations of Saturn's ring-plane crossing in August and November. Science 272, 509–516.
Oberc, P., 1996. Electric antenna as a dust detector. Adv. Space Res. 17, 105–110.
Pang, K.D., Voge, C.C., Rhoads, J.W., et al., 1984. The E ring of Saturn and satellite Enceladus. J. Geophys. Res.: Solid Earth 89 (B11), 9459–9470.
Porco, C.C., Helfenstein, P., Thomas, P.C., et al., 2006. Cassini observes the active south pole of Enceladus. Science 311, 1393–1401.
Schippers, P., Meyer-Vernet, N., Lecacheux, A., et al., 2014. Nanodust detection near 1 AU from spectral analysis of Cassini/Radio and Plasma Wave Science data. Geophys. Res. Lett. 41 (15), 5382–5388. doi:10.1002/2014gl060566.
Schmidt, J., Brilliantov, N., Spahn, F., et al., 2008. Slow dust in Enceladus' plume from condensation and wall collisions in tiger fracture. Nature 451, 685–688.
Showalter, M.R., Cuzzi, J.N., 1993. Seeing ghosts: Photometry of Saturn's G ring. Icarus 103 (1), 124–143.
Showalter, M.R., Cuzzi, J.N., Larson, S.M., 1991. Structure and particle properties of Saturn's E ring. Icarus 94, 451–473.
Sittler, E.C., Thomsen, M., Johnson, R.E., et al., 2006. Cassini observations of Saturn's inner plasmasphere: Saturn orbit insertion results. Planet. Space Sci. 54 (12), 1197–1210.
Smith, B.A., Soderblom, L., Beebe, R., et al., 1981. Encounter with Saturn: Voyager 1 imaging science results. Science 212 (4491), 163–191.
Spahn, F., Schmidt, J., Albers, N., et al., 2006. Cassini dust measurements at Enceladus and implications for the origin of the E ring. Science 311, 1416–1418.
Spahn, F., Albers, N., Hörning, M., et al., 2006. E ring dust sources: Implications from Cassini's dust measurements. Planet. Space Sci. 54 (9), 1024–1032.
Srama, R., Ahrens, T.J., Altobelli, N., et al., 2004. The Cassini cosmic dust analyzer. Space Sci. Rev. 114, 465–518.
Throop, H.B., Esposito, L.W., 1998. G ring particle sizes derived from ring plane crossing observations. Icarus 131 (1), 152–166.
Timmermann, R., Grün, E., 1991. Plasma emission from high velocity impacts of microparticles onto water ice. Origin and Evolution of Interplanetary Dust. Springer, Netherlands, pp. 375–378.
Tiscareno, M.S., 2013. Planetary rings. Planets, Stars and Stellar Systems. Springer, Netherlands, pp. 309–375.
Tsintikidis, D., Gurnett, D.A., Granroth, L.J., et al., 1994. A revised analysis of micron–sized particle detected near Saturn by the Voyager 2 plasma wave instrument. J. Geophys. Res. 99, 2261–2270.
Tsintikidis, D., Kurth, W.S., Gurnett, D.A., et al., 1995. Study of dust in the vicinity of Dione using the Voyager 1 plasma wave instrument. J. Geophys. Res. Space Phys. 100 (A2), 1811–1822.
Tsurutani, B.T., Clay, D.R., Zhang, L.D., et al., 2004. Plasma clouds associated with Comet P Borrelly dust impacts. Icarus 167 (1), 89–99. doi:10.1016/j.icarus.2003.08.021.
Van Allen, J.A., Thomsen, M.F., Randall, B.A., et al., 1980. Saturn's magnetosphere, rings, and inner satellites. Science 207 (4429), 415–421.
Verbiscer, A.J., Skrutskie, M.F., Hamilton, D.P., 2009. Saturn's largest ring. Nature 461 (7267), 1098–1100.
Wahlund, J.E., Boström, R., Gustafsson, G., et al., 2005. The inner magnetosphere of Saturn: Cassini RPWS cold plasma results from the first encounter. Geophys. Res. Lett. 32 (20), 986–989.
Waite, J.H., Combi, M.R., Ip, W.-H., et al., 2006. Cassini ion and neutral mass spectrometer: Enceladus plume composition and structure. Science 311, 1419–1422.
Wang, Z., Gurnett, D.A., Averkamp, T.F., et al., 2006. Characteristics of dust particles detected near Saturn's ring plane. Planet. Space Sci. 54, 957–966.
Ye, S.-Y., Gurnett, D.A., Kurth, W.S., et al., 2014. Properties of dust particles near Saturn inferred from voltage pulses induced by dust impacts on Cassini spacecraft. J. Geophys. Res.-Space Phys. 119 (8), 6294–6312. doi:10.1002/2014ja020024.
Zebker, H.A., Marouf, E.A., Tyler, G.L., 1985. Saturn's rings: Particle size distributions for thin layer models. Icarus 64 (3), 531–548.
Zebker, H.A., Tyler, G.L., 1984. Thickness of Saturn's rings inferred from Voyager 1 observations of microwave scatter. Science 223 (4634), 396–398.